Chinese Journal of Catalysis 47 (2023) 200–213

available at www.sciencedirect.com

ScienceDirect

journal homepage: www.sciencedirect.com/journal/chinese-journal-of-catalysis

Article

SCM-36 zeolite nanosheets applied in the production of renewable *p*-xylene from ethylene and 2,5-dimethylfuran

Duozheng Ma [a,b,c], Xiangcheng Li [b], Chuang Liu [b], Caroline Versluis [c], Yingchun Ye [b], Zhendong Wang [b,c,*], Eelco T. C. Vogt [c], Bert M. Weckhuysen [c,*], Weimin Yang [a,b,*]

[a] *School of Chemical Engineering, East China University of Science and Technology, Shanghai 200237, China*

[b] *State Key Laboratory of Green Chemical Engineering and Industrial Catalysis, Sinopec Shanghai Research Institute of Petrochemical Technology, Shanghai 201208, China*

[c] *Inorganic Chemistry and Catalysis group, Institute for Sustainable and Circular Chemistry and Debye Institute for Nanomaterials Science, Utrecht University, Universiteitsweg 99, 3584 CG Utrecht, the Netherlands*

ARTICLE INFO

Article history:
Received 24 October 2022
Accepted 25 November 2022
Available online 20 March 2023

Keywords:
Zeolite
Aluminosilicate
SCM-36
In-situ spectroscopy
Para-xylene
Biomass

ABSTRACT

Zeolites as solid acid materials have played important roles in industrial catalysis. The attempts to obtain new zeolite framework structures and related chemical compositions have never stopped, and may expand the application thereof. Using renewable bioderived molecules as starting feedstocks would be of great help in building a more circular carbon cycle. However, zeolites have only shown limited efficiency in the conversion or production of bioderived chemicals. In this work, we report on the synthesis of a new aluminosilicate zeolite named SCM-36 (Sinopec Composite Material No. 36) using tetramethylammonium hydroxide (TMAOH) with the presence of hexadecylpyridinium bromide hydrate (C_{16}PyBr) or octyltrimethylammonium chloride (OTMAC). The pore opening of this new zeolite material is about 0.6 nm, which is consistent with the size of 10 to 12 membered ring channel. SCM-36 possesses a nanoflower-like morphology with a thickness of ~20 nm. The SiO_2/Al_2O_3 molar ratio of the SCM-36 material is ranging from 21.2 to 36.6, with most Al incorporated into the zeolite framework structure. The acid strength of SCM-36 is not strong, as confirmed by various techniques, including NH_3-TPD, pyridine FT-IR, ex-situ confocal fluorescence microscopy and in-situ UV-Vis micro-spectroscopy. In the catalytic conversion of bio-derived 2,5-dimethylfuran (DMF) and ethylene into para-xylene (PX), H-SCM-36 zeolite showed better performance than the more traditional zeolites. The highest selectivity towards PX reached a value of ~93%. Besides, SCM-36 zeolite showed remarkable recyclability in the reaction.

1. Introduction

Zeolite materials are an essential class of crystalline microporous materials with industrial applications in separation, catalysis, ion exchange and adsorption [1–3]. Since the pioneering work of Barrer in the 1940s, the synthesis of new zeolites has been a constant interest in zeolite research [4]. To date, 247 different zeolite framework structures have been approved by the structure commission of the international zeolite association (IZA-SC) [5]. When used as catalytic materi-

* Corresponding author. E-mail: wangzd.sshy@sinopec.com (Z. Wang), B.M.Weckhuysen@uu.nl (B. Weckhuysen), yangwm.sshy@sinopec.com (W. Yang).

This work was supported by the National Natural Science Foundation of China (21972168, 21802168), China Scholarship Council (CSC), and China Petroleum & Chemical Corporation.
https://doi.org/10.1016/S1872-2067(22)64200-1

als, zeolites with nanoparticles, nanoneedles, nanosheets morphology and zeolites with hollow structures, have attracted great attention due to their improved diffusion properties compared with conventional ones of (sub-) micrometer size [6–10].

The syntheses of zeolites usually require the use of structure-directing agents (SDAs). Using inorganic cations, including alkali or alkaline-earth cations, as inorganic SDAs (ISDAs) enabled the formation of the first generation synthetic aluminosilicates with low Si/Al ratios [11]. Subsequently, the introduction of organic SDAs (OSDAs), such as quaternary ammonium cations or amines, favored the crystallization of high-silica zeolites. These N-containing amines or ammonium species acted as (1) SDAs, (2) local pH changers, and (3) pore fillers. The use of quaternary and diquaternary OSDAs, phosphorus-containing OSDAs, metal complexes and imidazolium derivatives resulted in the discoveries of many novel zeolites, and some of them possessed special channel systems like odd numbered-rings (11-, 15-rings), extra-large pores (16-, 18-, 20-, 28-, and 30-rings), and chiral pores [4,12].

There are examples of zeolite syntheses using two different organic SDAs [9,13–16], a combination of an OSDA and an ISDA [17], and a combination of an OSDA and zeolite seed [18–20]. It is capable to control structure formation [17], adjust morphology and compositions of framework atoms and crystalline phases [21,22]. In the cases of zeolite syntheses employing two OSDAs, the sizes of them are usually different, so that zeolites with complex channel systems and cavities were obtained [23–25]. The smaller SDA promoted the formation of small cages, while the larger one directed the formation of larger zeolite channels. Previous works have shown the critical roles of the SDAs in discovering new zeolites, modifying zeolite acid properties and modulating morphology [26]. The charge density mismatch (CDM) method is one such method using different SDAs that resulted in the syntheses of UZM-4, UZM-5 and UZM-9 [14,16]. Perez-Pariente and coworkers [27] synthesized nano-FER zeolite by employing a mixture of tetramethylammonium cation and benzylmethylpyrrolidinium. Cu-SSZ-13 zeolites were prepared by combining Cu-tetraethylenepentamine complex and *N,N,N*-trimethyl-1-adamantammonium [28]. High-silica ZSM-5 (MFI), ZSM-35 (FER), and ZSM-39 (MTN) zeolites were successfully synthesized by combing etramethylammonium and pyrrolidine as composite OSDA [29]. MFI zeolites with the different numbers of paired Al sites were synthesized in the presences of one OSDA and Na^+ [30].

Synthetic zeolites played important roles in the productions of many bulk chemicals. Para-xylene (PX) is one of them, which is mainly obtained from oil resource and used for the production of polyethylene terephthalate (PET) [31–35]. To address both economic and environmental concerns, the development of synthetic routes for renewable PX from biomass resources is highly desirable [36,37]. Great efforts have been devoted and synthetic pathways from bio-based reactants have been developed [31–35,37–40]. Noble metal-based catalysts were employed to synthesize PX from biomass-derived 4-methyl-3-cyclohexene-1-carboxaldehyde (4-MCHCA) [33,35]. A new procedure from bio-derived 2,5-dimethylfuran (DMF) and ethylene via Diels-Alder cycloaddition, followed by dehydration of the oxanorbornene intermediate, has recently been adopted (DMF-to-PX route) [31,40]. However, the reported selectivities towards PX from DMF achieved previously over Y zeolite and mesoporous MFI zeolite were about 75% [40,41]. Later, PX selectivity up to 90% was realized by using BEA [31], Zr-BEA [32], and phosphorous-containing zeolite [38]. Yet, complicated modification or post-treatment syntheses were needed. Therefore, it is still of great value to synthesize a new zeolite with high PX selectivity.

In this present work, we constructed a new synthetic system by using tetramethylammonium (TMAOH) as one OSDA, together with the presence of either hexadecylpyridinium bromide hydrate (C_{16}PyBr) or octyltrimethylammonium chloride (OTMAC). A new aluminosilicate zeolite, which we have coined as SCM-36 (Sinopec Composite Material No. 36), was synthesized. The X-ray powder diffraction pattern (XRD) of SCM-36 is, to the best of our knowledge, different from all reported ones and possessed a nanoflower morphology. The structure of SCM-36 is currently not determined yet, due to the lack of diffraction data. But the new material showed great potential in the production of bio-PX from DMF and ethylene.

2. Experimental

2.1. Materials

Ludox (HS-40 colloidal silica, 40 wt%, Sigma-Aldrich), Sodium aluminate ($NaAlO_2$, 45% Al_2O_3 and 35% Na_2O, TCI (Shanghai)), sodium hydroxide (NaOH, 99 wt%, TCI (Shanghai)), OTMAC (99.0 wt%, TCI (Shanghai)), TMAOH (25 wt% in water, TCI (Shanghai)), Hexadecylpyridinium bromide hydrate (C_{16}PyBr, 98 wt%, TCI (Shanghai)), Tetraethylammonium hydroxide (TEAOH, 20% aq. Solution, TCI (Shanghai)), Tetrapropylammonium hydroxide (TPAOH, 20% aq. Solution, TCI (Shanghai)), DMF (Alfa Aesar or Acros Organics, 98 wt%) and *n*-heptane (Alfa Aesar, 99 wt%), dicyclohexylamine (DCHA, 98 wt%, China Medicine (Group) Shanghai Chemical Reagent Co., Ltd.), hexamethyleneimine (HMI, 99wt%, TCI (Shanghai)), 4-fluorostyrene (99 wt%, Sigma-Aidrich), 4-methoxystyrene (97 wt%, Sigma-Aidrich) and the deionized water prepared in our laboratory were used as starting materials without any further purification.

2.2. Synthesis of SCM-36 zeolite

The new zeolite SCM-36 materials were synthesized as follows. When TMAOH and C_{16}PyBr were used as co-OSDAs, the gel molar composition was 1.0 SiO_2:0.04 Al_2O_3:0.30 NaOH:0.15 C_{16}PyBr:0.15 TMAOH:25 H_2O. In a typical run, 0.635 g aqueous NaOH solution (30% in water) was added into 8.18 g deionized water, followed by the addition of 0.218 g $NaAlO_2$. After stirring for 10 min at room temperature, 1.32 g of aqueous TMAOH solution and 1.02 g of C_{16}PyBr were added, and the mixture was stirred for 20 min. When TMAOH and OTMAC were used as co-OSDAs, starting gel with the composition of 1.0 SiO_2:

(0.0167–0.028) Al_2O_3: 0.30 NaOH: 0.15 OTMAC: 0.15 TMAOH: 25 H_2O was used. The resulting mixture was transferred to a 25-mL Teflon-lined autoclave within a conviction rotation oven and maintained at 160 °C for 5 d. After the autoclave was cooled to about 25 °C, the zeolite solid material was separated by filtration, washed for 3 times with deionized water, and dried overnight at 100 °C under air. Calcination of as-synthesized SCM-36 zeolite was carried out in air at 550 °C for 6 h resulting in removing the OSDA occluded in the pores. The obtained samples were designated as SCM-36(*n*), where "*n*" stands for the SiO_2/Al_2O_3 molar ratio of the synthesis gel if there is no special description.

The protonated forms of SCM-36 zeolites materials were obtained via ion exchange by adding 1.0 g of calcined zeolite into 25 mL of 0.5 mol/L NH_4Cl solution. The ion exchange process was repeated three times while being stirred at 80 °C for 2 h. The resulting samples were then separated, dried, and calcined at 550 °C for 6 h before being denoted as H-SCM-36.

2.3. Other catalyst preparation

Beta zeolite (SiO_2/Al_2O_3=20) was synthesized with synthetic gel composition of 1.0 SiO_2:0.05 Al_2O_3:0.1 NaOH:0.35 TEAOH: 0.15 NH_4F:12 H_2O. In a typical run, 0.29 g $NaAlO_2$ and 7.05 g tetraethylammonium hydroxide solution (20% in water) were added into 3.40 g deionized water and followed by the addition of 0.154 g NH_4F. After thorough stirring, 4.11 g of HS-40 colloidal silica was added dropwise. Finally, the mixture was encapsulated into a 50-mL Teflon-lined autoclave within a conviction rotation oven for dynamic crystallization at 170 °C for 3 d.

ZSM-5 zeolite (SiO_2/Al_2O_3 = 40) was synthesized with gel composition 1.0 SiO_2:0.025 Al_2O_3:0.20 NaOH:0.20 TPAOH:25 H_2O. In a typical run, 0.118 g NaOH and 4.20 g tetrapropylammonium hydroxide solution (20% in water) were added into 7.44 g deionized water and followed by the addition of 0.11 g $NaAlO_2$. After thorough stirring, 3.10 g of HS-40 colloidal silica was added dropwise. Finally, the mixture was encapsulated into a 50-mL Teflon-lined autoclave within a rotation oven (20 r/min) for dynamic crystallization at 160 °C for 5 d.

SCM-1 (MWW type zeolite) (SiO_2/Al_2O_3 = 15) was prepared according to our published work [42]. In a typical run, NaOH, $NaAlO_2$, dicyclohexylamine (DCHA) and hexamethyleneimine (HMI) were added to deionized water in turn under stirring. And then the HS-40 was added dropwise. The resulting gel with compositions of 1.0 SiO_2:1/30 Al_2O_3:0.10 NaOH:0.30 HMI:0.4 DCHA:18 H_2O were transferred into the Teflon-lined stainless-steel autoclaves for dynamic crystallization (20 r/min) at 150 °C for 5 d.

A commercial USY zeolite (SiO_2/Al_2O_3 = 23) and SAPO-34 (P/Al = 1.8) were purchased from TOSOH Corporation.

The protonated catalysts were obtained *via* ion exchange. Before catalytic test, the catalysts were heated at 550 °C for 6 h under dried airflow with an online drierite tube to remove moisture present in the gas.

2.4. Characterization

2.4.1. Chemical composition, structural and textural properties

In-situ XRD patterns were recorded on a D8 Advance X-ray diffractometer using Cu K_α radiation (λ = 1.54 Å) operated at 40 kV and 40 mA. Samples (SCM-36) were packed in air under ambient pressure in a rotating borosilicate glass tube with an outer diameter of 0.5 mm and heated from 30 to 700 °C. The data were collected every 50 °C from 30 to 700 °C. *Ex-situ* XRD patterns were recorded on a on a PANalytical X'Pert PRO diffractometer. The heights of zeolite nanosheets were acquired by Atomic Force Microscopy (AFM) with a NT-MDT NTEGRA Spectra upright instrument working in tapping mode under ambient conditions. AFM images were acquired using a diamond tip (DP14/SCD/AIBS, F = 5.7 N/m, MikroMash, resonance frequency ≈ 160 kHz) at a scan rate of 0.6 Hz and 512 lines/scan. The data were post-processed and analyzed with Gwyddion. Statistical distribution of thickness of zeolite materials by the AFM measurements from a total of 62 valid nanosheet thickness data in Fig. 3(d). Scanning electron microscopy (SEM) measurements were performed on a Hitachi S-4800 field-emission scanning electron microscope (Hitachi, Japan) with an acceleration voltage of 3.0 kV. The High-resolution transmission electron microscopy (HRTEM) images and Transmission Electron Microscopy (TEM) images and fast Fourier transform (FFT) diffractogram images were obtained by a FEI Titan Cubed Themis G2 300 electron microscope operated at 300 kV, with a DCOR+ probe corrector. Elemental analyses of the samples were performed on an inductively coupled plasma-atomic emission spectroscopy (ICP-AES) on a Varian 725-ES instrument after dissolving the samples in HF solution. Thermogravimetric analysis (TGA) data was collected in the temperature range of 30–800 °C on a thermogravimeter (STA 449F3, Netzsch) under N_2 (40 mL/min) at a heating rate of 10 °C/min, and the effluent was monitored by the mass spectrometer (QMS403). The mass range of m/z 16–166 was scanned. N_2 and Ar adsorption-desorption isotherms were measured at 77 K on an ASAP2020 M TriStar 3000 instrument after the sample was degassed at 300 °C for 4 h. The Brunauer-Emmet-Teller (BET) area was calculated from the adsorption data obtained in the relative pressure (p/p_0) range of 0.01–0.1, and the total pore volume was calculated from the amounts adsorbed at a relative pressure of approximately 0.99. Surface, external surface area and micropore volume were collected using t-plot method (p/p_0 = 0.41–0.60). The pore size distribution of the samples was calculated by the Horvath-Kawazoe (H-K) method.

2.4.2. Nuclear magnetic resonance (NMR)

The liquid ^{13}C NMR spectrum was recorded on a Bruker AV-400 spectrometer. ^{13}C, ^{29}Si and ^{27}Al solid-state magic angle spinning nuclear magnetic resonance (MAS NMR) measurements were performed on a JNM-ECZ500R/S1 (JEOL) spectrometer under one-pulse condition. The ^{13}C MAS NMR spectra were recorded at a ^{13}C frequency of 125.765 MHz and a spinning rate of 18.0 kHz with a π/2 rad pulse length of 5.0 μs, ^{13}C chemical shifts were reported relative to adamantane (ADA). The ^{29}Si MAS NMR spectra were obtained with a ^{29}Si frequency of 99.367 MHz and a spinning rate of 6.0 kHz with a π/2 rad

pulse length of 7.6 μs, the ^{29}Si chemical shifts were reported relative to a 4,4-dimethyl-4-silapentane-1-sulfonic acid (DSS) solution. The ^{27}Al MAS NMR spectra were recorded at a ^{27}Al frequency of 130.322 MHz and a spinning rate of 18.0 kHz with a π/2 rad pulse length of 1.4 μs, the ^{27}Al chemical shifts were referenced to an $Al(NO_3)_3$ solution (1 mol/L).

2.4.3. Acid sites characterization

NH_3-temperature programmed desorption (NH_3-TPD). The amount of acid sites were determined by NH_3-TPD on an Altamira AMI-3300 chemisorption instrument with a thermal conductivity detector (TCD). Around 10 mg catalyst was tested, and the temperature-programmed desorption/decomposition of isopropyl amine was carried out with a rate of 10 °C/min to 600 °C.

In-situ pyridine FT-IR spectroscopy. The number of Lewis and Brönsted acid sites was measured by Fourier transform-infrared (FT-IR) spectroscopy on a Nicolet 5700 FT-IR spectrometer. The samples preparation was performed using the self-supporting wafer technique. Determination of the Brönsted/Lewis acid site ratio by integrating the absorbance bands corresponding to the Brönsted acid site (~1545 cm^{-1}) and Lewis acid site (~1454 cm^{-1}) and applying molar extinction coefficients (1.67 and 2.22 cm μmol^{-1}, respectively) [43]. The weight of wafer was about 15.0 mg.

In-situ CO FT-IR spectroscopy. When using CO as a probe molecule, *in-situ* FT-IR spectra was obtained by using a Jasco FT-IR 7000 spectrometer equipped with an MCT detector at a 4 cm^{-1} resolution. Approximately 30 mg sample was pressed into a 20 mm diameter self-supporting disk and placed in a quartz cell connected to a conventional closed gas circulation system. The sample disk was evacuated and pretreated at 500 °C for 1 h. The temperature was then decreased to –120 °C in the evacuated state. Before adsorption experiments, the FT-IR spectra of blank samples were measured by evacuation at –120 °C and were used as background spectra. Then, 0.85 mmol of CO was introduced to the sample. FT-IR spectra were measured with the CO dosage increased to 24 mmol; the CO pressure was changed from 0.001 to 10 mbar. Unless otherwise mentioned, the shown IR spectra were resulted from subtraction of background.

In-situ UV-Vis micro-spectroscopy. The microscope set-up is based on an Olympus BX41 upright microscope with a 50 × 0.5 NA-high working distance microscope objective (NA: numerical aperture). The light source was a 75 W tungsten bulb. A CCD video camera (ColorView IIIu, Soft Imaging System GmbH) and an optical fiber mount were mounted on the microscope's 50/50 double-viewport tube. The microscope and the CCD UV/Vis spectrometer were connected by a 200 mm-core fiber (AvaSpec-2048TEC, Avantes). All experiments were performed at ambient pressure in a *in-situ* cell (FTIR600, Linkam Scientific Instruments) with a temperature controller (Linkam TMS 94). The 10 mg of zeolite was compressed into a pellet and was heated up to 100 °C at a rate of 10 °C/min and kept at this temperature for 1 h under an inert atmosphere with nitrogen. Then 15 ml of 4-fluorostyrene or 4-methoxystrene was added. After waiting for 5 min, UV-Vis spectra were taken every 10 s with an integration time of one hundred milliseconds.

Confocal fluorescence microscopy setup. The *ex-situ* confocal fluorescence microscopy (CFM) studies of the spent samples after styrene derivatives oligomerization were performed on a confocal fluorescence microscopy set-up. A Nikon Eclipse 90i microscope, equipped with a pin hole to block out-of-focus light, was utilized for imaging, and dichroic mirrors with the appropriate laser line wavelength were also used. The microscope had a Nikon A1 scan head that could accommodate the optics, which connected the microscope to fiber optics for excitation and emission light. The Nikon A1 system was equipped with an A1-DUS spectral detector unit, with 32 channels and a wavelength resolution of 10 nm designed to collect emission light in the wavelength detection range of 430-750 nm, and a Nikon 60/0.30 objective. The 3-D volumes were created by 3D reconstructing the individual photographed slices and were displayed as top-view images. In order to prevent channel overlap, the emission was detected using three photomultiplier tubes in the wavelength ranges of 425–475, 510–550, and 575–635 nm.

2.4.4. Catalytic testing

The catalytic conversion of DMF and ethylene was conducted in a 100 mL Teflon-lined stainless-steel autoclaves. In a typical run, ~1.2 ± 0.1 mol/L of DMF (1.0 g), *n*-heptane (20 mL) and H-form zeolite (1.0 g) were enclosed in the reactor, which was then sealed and purged three times with ethylene and charged to an initial pressure of 2.0 MPa with ethylene. The reactor was then stirred at 600 r/min, heated to 250 °C and held for 24 h under vigorous mixing. When the reaction was finished, the reactor was rapidly cooled down and the used zeolite was removed by filtration. The reaction product was analyzed using GC-MS (Agilent 7890A) and GC (Agilent 7890B), both columns equipped with HP-INNOWAX columns. The used zeolite was regenerated by calcination in air and then tested again under the same condition. Decane was used as an internal standard.

The conversion of DMF and selectivity and yield to the products are defined as follows:

$$X_{DMF}\,(\%) = (C_{DMF,t0} - C_{DMF,t}) \times 100\% / C_{DMF,t0}$$

$$\text{Selectivity}_{\text{product } i}(\%) = C_i \times 100\% / (C_{DMF,t0} - C_{DMF,t})$$

where t is the duration of time after ethylene was added to the reactor, and C_i is the concentration of the products, i.

p-Xylene (PX), over alkylated products (OAB), 2-5-hexanedione (HDO) and methyl cyclopentenone (MCP) were the main products in the reaction system and the by-products were named as oligomers as many literatures reported before, therefore the reaction imbalance belongs to the formation of oligomers.

The solid yield was calculated by the following formula:

$Y(\%)$ = calcined zeolite powder $\times 100\% / (SiO_2 + NaAlO_2 + NaOH)_{gel}$

3. Results and discussion

3.1. Structural characterization

Fig. 1 shows the XRD and *in-situ* XRD patterns of as-made and calcined/heated SCM-36(35) (35 stands for the SiO_2/Al_2O_3 molar ratio). The as-synthesized SCM-36 zeolite material shows six prominent characteristic diffraction peaks, and five of them maintained during calcination treatment (Fig. 1(a)) except for the peak at 2θ = 17° (Fig. 1(a), top). After calcination at 550 °C, the first diffraction peak shifted from 8.90° to 9.70°, indicating a decrease of the unit-cell (UC) parameter due to the condensation of silica layers by removal of the OSDAs [44]. It seems the framework of SCM-36 is constructed by layered structure. When SCM-36 zeolite was heated from 30 to 700 °C, the first diffraction peak gradually shifted to higher angle and reached 10.1° at 700 °C (Fig. 1(b)). The diffraction peaks centered at around 19.2° and 26° also shifted slightly to higher values. Intensities of most diffraction peaks decreased significantly at 450 °C, which is likely due to the condensation of Si-OH groups and the removal of organic species (Fig. 1(c)). Interestingly, the TG and DTA curves show that the decomposition of organics first took place at around 450 °C. We have searched the Database of all Framework Type Codes and Disordered Zeolite Structures, but found no XRD patterns of all known zeolites that match the XRD pattern of SCM-36 [5].

The syntheses of SCM-36 zeolites were optimized for both co-OSDAs systems (Table S1 and Fig. S1). When TMAOH and C_{16}PyBr were used, pure SCM-36 zeolites were obtained with SiO_2/Al_2O_3 ratio ranging from 25 to 30 (Fig. S1(A)). Omega zeolite and quartz appeared as impurities for synthetic runs with SiO_2/Al_2O_3 ratios below 25 and above 30, respectively. Interestingly, when TMAOH and OTMAC were used, SOD zeolite, SCM-36, and RUT zeolite were observed with the increase of SiO_2/Al_2O_3 ratio from 15 to 70 (Fig. S1).

All the SCM-36 samples show nanosheet morphology regardless of whether the second OSDA is C_{16}PyBr or OTMAC (Fig. S2). Figs. 2(a) and (b) show the SEM images of as-synthesized and calcined SCM-36(35) materials, both exhibit aggregates of nanosheets with flower-like morphology. TEM-EDX mapping confirms the homogeneous distribution of Al, Na and Si elements and no Al enriched zone was observed (Figs. 2(c) and (d)). TEM images of the SCM-36(35) sample again showed the nanosheet morphology (Fig. 2(e)). The thickness of one nanosheet is about 18.24 nm, and the crystal was constructed by stacking of 12 layers (Fig. 2(f)). HRTEM image and FFT diffractogram image (Figs. 2(g) and (h)) confirmed the blurry lattice fringes and arrangement of crystal structures. Attempts to improve the quality did not pay back. Three-dimensional rotation electron diffraction (3D-RED) was also carried out, hoping to realize data collection and processing to determine the structure of SCM-36. However, only limited information could be extracted due to the sensitivity of the nanosheet crystals to electron beam. The layered structure of SCM-36 zeolite might be similar with that of FER zeolite. But obvious differences in XRD patterns of SCM-36, conventional FER (c-FER) and nanosheet FER (NS-FER) zeolites were observed (Fig. S3). Three-dimensional electron diffraction (3D ED), an important characterization technique used for understanding zeolite crystals, was adopted to investigate the crystal structure of SCM-36. However, it ended in failure due to electron beam damage to SCM-36 and not enough diffraction data were collected. We also collected SCM-36 sample after crystallization for 30 d. Still, it is beam sensitive due to the ultra-thin nanosheet crystals. To solve the structure of SCM-36 may take quite a long time. More efforts would be devoted in the future to obtain better sample and more diffraction data.

The solution of the exfoliated layers obtained by the experimental part of the procedure was diluted 100 times and used for AFM measurements. A 3D-AFM mountain map with a step

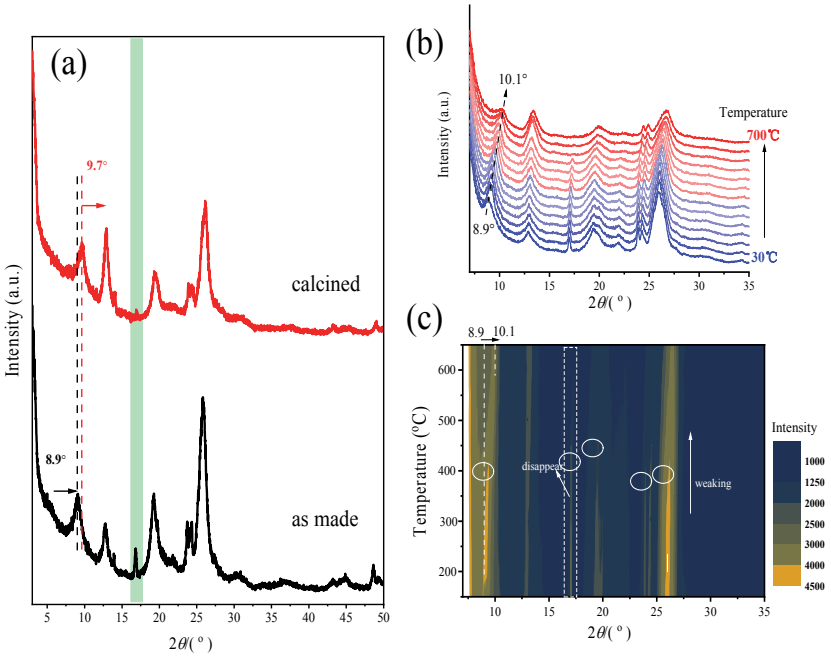

Fig. 1. (a) XRD patterns of as-made SCM-36 (bottom) and calcined SCM-36 at 550 °C (top); *In-situ* XRD patterns were recorded while heating the synthesized material from 30 to 700 °C (b) and its corresponding 'heatmap' (c). The patterns were recorded with Cu K_α-radiation.

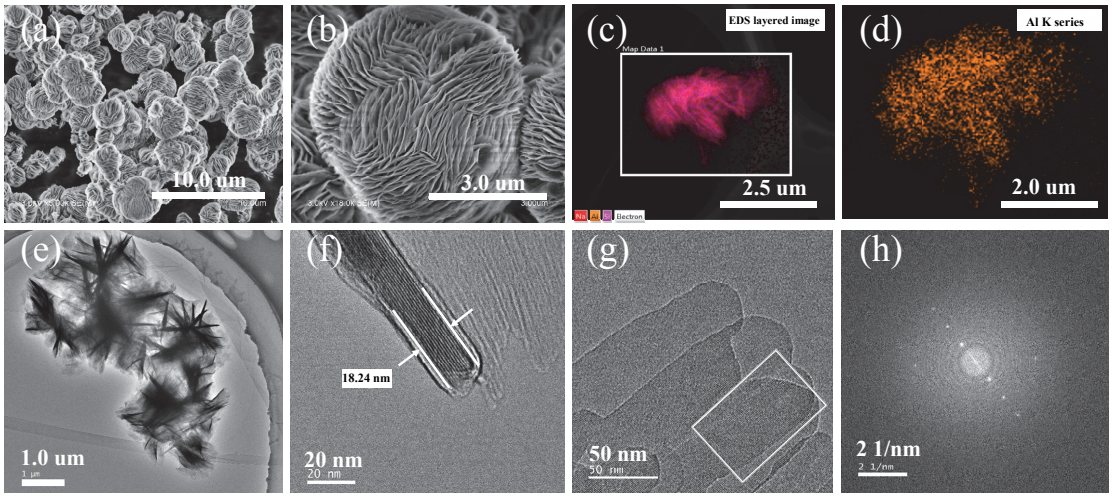

Fig. 2. SEM images of as-synthesized (a) and calcined (b) SCM-36(35) zeolite. TEM-EDX mapping of all chemical elements (c) and its Al element (d). HRTEM images of calcined SCM-36(35) (e–g) and its FFT pattern (h).

gradient reveals the approximate thickness of each layer of SCM-36(35). The heights of the cross-section in Fig. 3(a) and (b) along the red dashed lines show layer thickness in the range of 6.9–14.9 nm (Fig. 3(c)). This indicates that the thickness of the SCM-36 nanosheet is relatively uniform, and the 14.9 nm thickness layer is most likely the result of stacking of two pieces of nanosheets. Statistical distribution gives the thickness of nanosheets centered ~10.0–12.0 nm (Fig. 3(d)), as derived from 62 times AFM measurements for selected nanosheet samples. The thickness of the SCM-36(25) nanosheets which directed by TMAOH and C_{16}PyBr also fell within this interval (Fig. S4).

The microporous nature of SCM-36(35) was confirmed by N_2 and Ar adsorption-desorption, with micropore size centers at 0.59 and 0.67 nm, corresponding to 10–12 membered ring openings (Fig. 4(a) and (b)) [5,45]. SCM-36 possesses relatively large specific surface area of 348 m^2/g and mesopores with pore volume up to 0.48 (cm^3/g) (Table 1). Samples obtained from gels with different SiO_2/Al_2O_3 ratios show similar adsorption-desorption isotherms (Fig. S5), and small differences in micropore areas and pore volumes (Table 1). The bulk SiO_2/Al_2O_3 molar ratios of SCM-36 zeolites were different from those in the corresponding starting gels. The bulk SiO_2/Al_2O_3 ratios increased with the increase of starting SiO_2/Al_2O_3 ratios

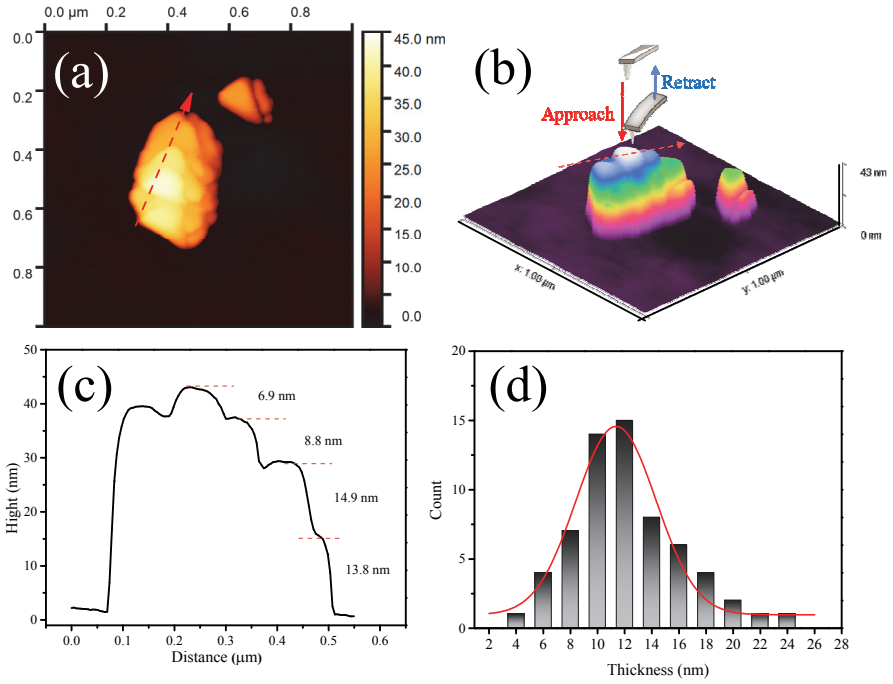

Fig. 3. AFM topography image of the layers deposited from ethanol solution of calcined SCM-36(35) zeolite (a) and its corresponding 3D AFM mountain image (b), cross-section profiles extracted from (a) or (b) marked by the dashed red line (c). Statistical distribution of thickness of SCM-36(35) by the AFM measurements from a total of 62 valid nanosheet thickness data (d).

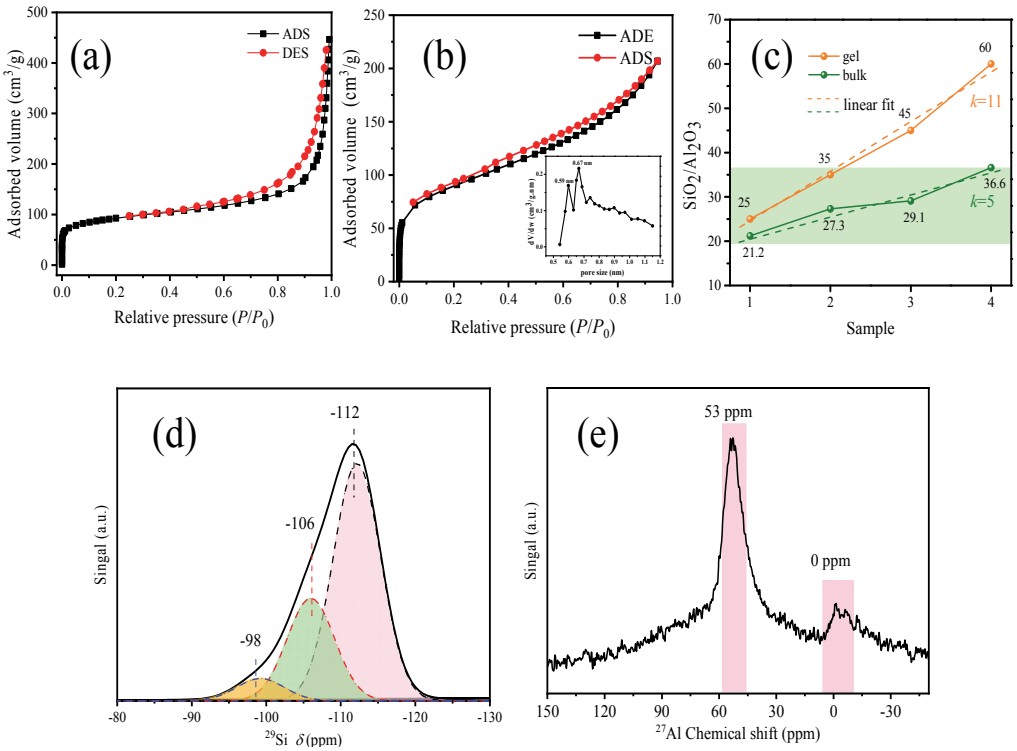

Fig. 4. N_2 (a) and Ar (b) adsorption-desorption isotherms and micropore size distribution (by the Horvath-Kawazoe method of calcined SCM-36(35); (c) SiO_2/Al_2O_3 ratios in synthetic gels and in SCM-36 solid products. ^{29}Si (d) and ^{27}Al (e) NMR spectra of calcined SCM-36(35) zeolite.

Table 1
Structural features of SCM-36(n) zeolites [a].

Sample	SiO_2/Al_2O_3		Yield	A_{BET} [e]	$A_{ext.}$ [e]	$A_{micro.}$ [e]	V_{total} [f]	$V_{micro.}$ [f]
	Gel	Bulk [d]	(%)	(m^2/g)	(m^2/g)	(cm^2/g)	(cm^3/g)	(cm^3/g)
SCM-36(25) [b]	25	21.2	85	355	121	234	0.62	0.10
SCM-36(35) [c]	35	27.3	80	348	138	210	0.57	0.09
SCM-36(45) [c]	45	29.1	76	319	105	214	0.49	0.093
SCM-36(60) [c]	60	36.6	64	296	92	204	0.45	0.089

[a] All samples were synthesized using the gels with molar compositions of $TMAOH/SiO_2$ = 0.15, $NaOH/SiO_2$ = 0.30, H_2O/SiO_2 = 25. The second OSDA is [b] $C_{16}PyBr/SiO_2$ = 0.15 and [c] OTMAC = 0.15. [d] Determined by ICP-AES. [e] Determined by the Brunauer-Emmett-Teller (BET) method. [f] Determined by *t*-plot method.

in gels, and the increase rate in solid products (k = 5) was much lower than that in the gel (k = 11) (Fig. 4(c)). For sample SCM-36(35), the bulk SiO_2/Al_2O_3 ratio determined by ICP-AES was 27.3 (Table 1), and those given by TEM-EDX mapping (Fig. 2(c)) and ^{29}Si NMR spectrum (Fig. 4(d)) were 24.4 and 23.8, respectively. The product yield gradually decreased with the increase of SiO_2/Al_2O_3 ratio in gel (Table 1). The differences indicated that only part of the Si species was involved in the zeolite product, while the rest existed in the solution.

The ^{29}Si NMR spectrum of the calcined SCM-36(35) material shows a distinct peak centered at –112 ppm, which is consistent with the four-connected Si environment characteristics of typical zeolite materials (Fig. 4(d)) [46–49]. The incorporation of Al into the zeolite framework is confirmed by the clear resonance at ~53 ppm corresponding to the tetrahedrally coordinated framework Al species (Fig. 4(e)). The signal at 0 ppm attributed to the characteristic of octahedral non-framework Al species was also observed. While zeolites obtained in the starting gels with higher SiO_2/Al_2O_3 ratios (45 and 60) possessed few non-framework Al species (Fig. S6).

As shown in Figs. 5(a) and (c), TMA^+ was occluded in the pores of the as-synthesized zeolite. A small amount of $C_{16}PyBr$ and OTMAC were impeded in SCM-36(25) and SCM-36(35) zeolite channels, respectively. Organic species decomposition behavior was investigated in TG/DTA (Fig. 5(b) and (d)). The weight loss in the low-temperature region (25–200 °C) is mainly attributed to the desorption of physically adsorbed water. In the medium-temperature region (200–480 °C), the weight loss of SCM-36(25) and SCM-36(35) is 8.5% and 4.1%, respectively. It is worth noting that the relative molecular mass of $C_{16}Py^+$ (304.44) is almost twice the mass of $OTMA^+$ (172.28). The weight loss in the high-temperature region of 480–750 °C is originated from the removal of the occluded TMA^+ species [50]. TMA^+ is essential for the crystallization of SCM-36, while $C_{16}Py^+$ and $OTMA^+$ seems to act as pore filler, and regulate the Si/Al of the zeolite framework as well.

3.2. *Estimation of the amount of acid sites by NH_3-TPD*

Two NH_3-desorption peaks in the TPD experiments corre-

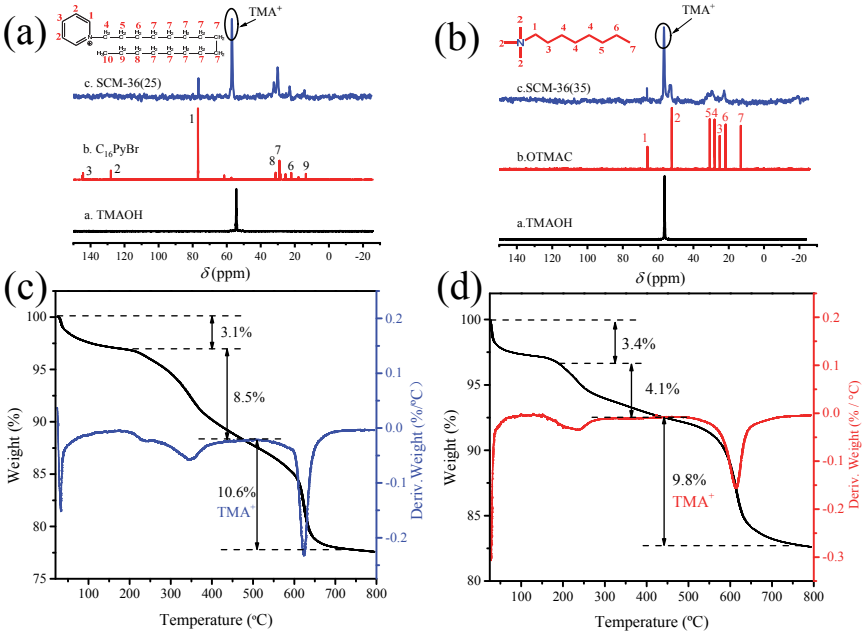

Fig. 5. (a) ^{13}C liquid NMR spectra of C_{16}PyBr and TMAOH, ^{13}C solid-state MAS NMR of SCM-36(25). (b) TG/DTA curves of SCM-36(25). (c) ^{13}C liquid NMR of OTMAC and TMAOH, ^{13}C solid-state MAS NMR of SCM-36(35). (d) TG/DTA curves of SCM-36(35).

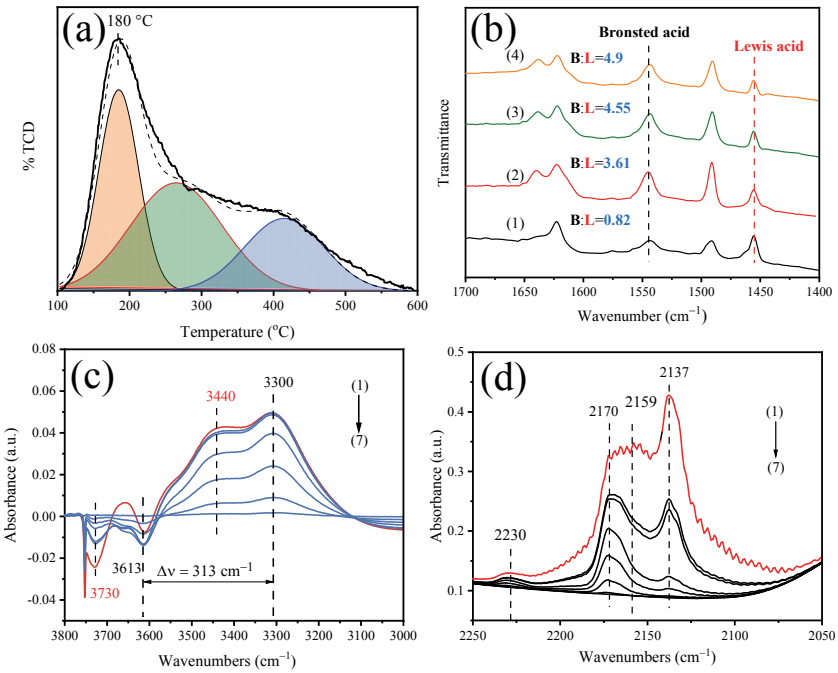

Fig. 6. (a) NH_3-TPD profiles of H-SCM-36(35). (b) Pyridine-adsorbed FT-IR spectra (measured at 150 °C) of SCM-36 zeolites synthesized with starting SiO_2/Al_2O_3 gel compositions of ratios of 25 (1), 35 (2), 45 (3), and 60 (4). OH-stretch region (c) and CO-stretch region (d) of FT-IR spectra of SCM-36(35) zeolite. In (c) and (d), the sample was measured at 300 °C at P_{CO} = 10.0 under pressure of P_{CO} = 10.0 (1), 1.0 (2), 0.5 (3), 0.1 (4), 0.05 (5), 0.01(6) and 0.001 (7) mbar.

sponding to weak and medium-strong acid sites were observed at ~180 and 380 °C, respectively (Fig. 6(a)). The NH_3-TPD curve is not adequately resolved in two different temperature domains, which is characteristic of the overlap of several components over a relatively wide temperature range. This means that the strengths of Brönsted acid sites are heterogeneous in nature [51]. SCM-36 is a weak acid-dominated material, the proportion of weak acid sites exceeds 75% of the total acid sites (Table 2). With the decrease of Al content, both weak acid and total acid site decreased, except for that of SCM-36(25) that possesses the most acid sites, the acid amounts of the other samples are comparable due to their similar bulk SiO_2/Al_2O_3 (Table 2 and Fig. S7).

3.3. Evaluation of acid properties by in-situ Fourier transform infrared spectroscopy using pyridine and CO as probe molecules

Table 2
Acidic properties of SCM-36 given by NH_3-TPD and pyridine adsorbed FT-IR spectroscopy.

Sample	NH_3-TPD[a] (μmol/g)		Brönsted acid[b] (μmol/g)			Lewis acid[b] (μmol/g)		
	Weak+Medium	Total	150 °C	250 °C	350 °C	150 °C	250 °C	350 °C
SCM-36(25)	657	872	40	19	5	36	19	6
SCM-36(35)	512	674	85	73	44	24	15	9
SCM-36(45)	495	635	89	46	17	19	9	7
SCM-36(60)	477	605	97	58	19	15	13	8

[a] Measured using NH_3-TPD; [b] Measured using pyridine adsorbed FT-IR spectroscopy.

FT-IR spectra of pyridine-adsorbed SCM-36 zeolites are presented in Fig. 6(b), and the calculated amounts of Brönsted and Lewis acid sites are listed in Table 2. The peaks at 1540 and 1445 cm^{-1} are representative of Brönsted and Lewis acid sites, respectively, and the peak at 1490 cm^{-1} represents both Lewis and Brönsted acid sites [43,52]. The amount of Brönsted acid sites increases significantly with increasing SiO_2/Al_2O_3 ratio, while the amount of Lewis acid sites decreases (Fig. S8). The Brönsted/Lewis ratio of SCM-36(25) was 0.82, while those of SCM-36(35), SCM-36(45) and SCM-36(60) were much higher up to 3.61, 4.55 and 4.90, respectively (Fig. 6(b)).

The acid strength of SCM-36 zeolite material was further investigated by *in-situ* FT-IR spectroscopy after low-temperature CO adsorption. The number and strength of Brönsted acid sites can be assessed by the OH-stretching region [53]. All protonic sites are saturated with CO at −130 °C, thus resulting to a downshift in the FT-IR band of the acidic Si(OH)Al hydroxyls due to their hydrogen bonding with the CO molecules. Therefore, the $\Delta\upsilon$(CO···OH) can be used as a measure of the acid strength. Four distinct peaks are visible in the OH-region of the FT-IR spectrum (Fig. 6(c)). The peak at 3730 cm^{-1} was attributed to isolated Si-OH groups, and the broad peak at around 3440 cm^{-1} was corresponding to silanol nets [54,55]. Upon the adsorption of CO, the peak at 3613 cm^{-1} which is assigned to an OH-group corresponding to Brönsted acid shifted to 3300 cm^{-1} with $\Delta\upsilon$(CO···OH) = 313 cm^{-1}. SCM-36(45) showed a wavenumber shift of $\Delta\upsilon$(CO···OH) = 313 cm^{-1} (Fig. S9(a)). The strength of Brönsted acid of SCM-36 zeolite is comparable to that of ZSM-5 (SiO_2/Al_2O_3 = 108, $\Delta\upsilon$ = 340 cm^{-1}) [56] and slightly higher than those of MOR (SiO_2/Al_2O_3 = 26, $\Delta\upsilon$ = 294 cm^{-1}) [57], beta (SiO_2/Al_2O_3 = 38, $\Delta\upsilon$ = 309 cm^{-1}) [58] and Y (SiO_2/Al_2O_3 = 5.8, $\Delta\upsilon$ = 296 cm^{-1}) [59] zeolites.

The CO-stretch region can be used to assess the presence of both Brönsted and Lewis acid sites since it can provide the information on how the C–O bond is perturbed upon adsorption of CO (gas phase absorbance at 2143 cm^{-1}) [54,55]. For zeolite H-SCM-36(35) (Fig. 6(d)), three distinct peaks in the CO region, i.e., at 2170, 2159, and 2137 cm^{-1} were observed. These peaks were attributed to CO interacted with Brönsted acid sites, silanol groups, and physiosorbed CO, respectively. While the peak at 2230 cm^{-1} is attributed to Lewis acid sites. These peaks indicated the existences of both Brönsted acid sites and Lewis acid sites in SCM-36(35), and in SCM-36(45) as well (Fig. S9(B)).

3.4. Brönsted acidity and reactivity studied by in-situ UV-Vis microscopy and ex-situ confocal fluorescence microscopy

The oligomerization of 4-methoxystyrene can be catalyzed by all acid sites present in the zeolite material, resulting in the formation of fluorescent oligomer products. However, 4-fluorostyrene is more electronegative, and hence is a less reactive compound and its oligomerization would occur only over strong(er) Brönsted acid sites [60,61]. The rate constants for the oligomerization of 4-methoxystyrene and 4-fluorostyrene over ZSM-5 zeolites were 0.05 and 0.007 k[mol^{-1} s^{-1}], respectively, further indicating the difference in their sensitivity towards the strength of Brönsted acid sites [62].

Potential reaction species and mechanisms have been postulated for the acid-catalyzed oligomerization of 4-methoxystyrene and 4-fluorostyrene (Fig. S10) [60,61]. When 4-methoxystyrene was used as a probe molecule, both SCM-36(35) and ZSM-5 (SiO_2/Al_2O_3 = 40) zeolites were highly active. The UV-Vis spectra of SCM-36 show the appearance of absorption bands at 585 nm (Fig. 7(a)), which are attributed to the presence of linear allylic carbocations. The corresponding CFM image shows the orange-yellow fluorescence of the mac-

Table 3
Catalytic performances of some conventional zeolites and the newly synthesized SCM-36 zeolite in conversion of DMF and ethylene to produce PX.

Catalyst	SiO_2/Al_2O_3[a]	DMF conversion (%)	Selectivity (%)				
			PX	OAB	HDO	MCP	Oligomers
SCM-1 (MWW)	15	>99	63	18	4	4	11
Beta	20	>99	75	9	5	3	8
USY	23	>99	81	5	3	2	9
ZSM-5	40	93	72	11	3	2	12
SAPO-34	0.5[b]	>99	56	6	23	7	8
SCM-36(25)	21.2	>99	86	3	3	2	6
SCM-36(35)	27.3	95	91	1	2	1	5
SCM-36(45)	29.1	>99	89	2	3	2	4
SCM-36(60)	36.6	98	93	1	2	0	4

[a] Measured using ICP-AES, SAR is SiO_2/Al_2O_3 ratio in the solid sample. [b] SAPO-34: P/Al=1.0. Reaction: ~1.2±0.1 mol/L of DMF (1.0 g), *n*-heptane (20 mL) and zeolite (1.0 g) enclosed in the reactor and then heated to 250 °C for 24 h at 2.0 MPa with ethylene.

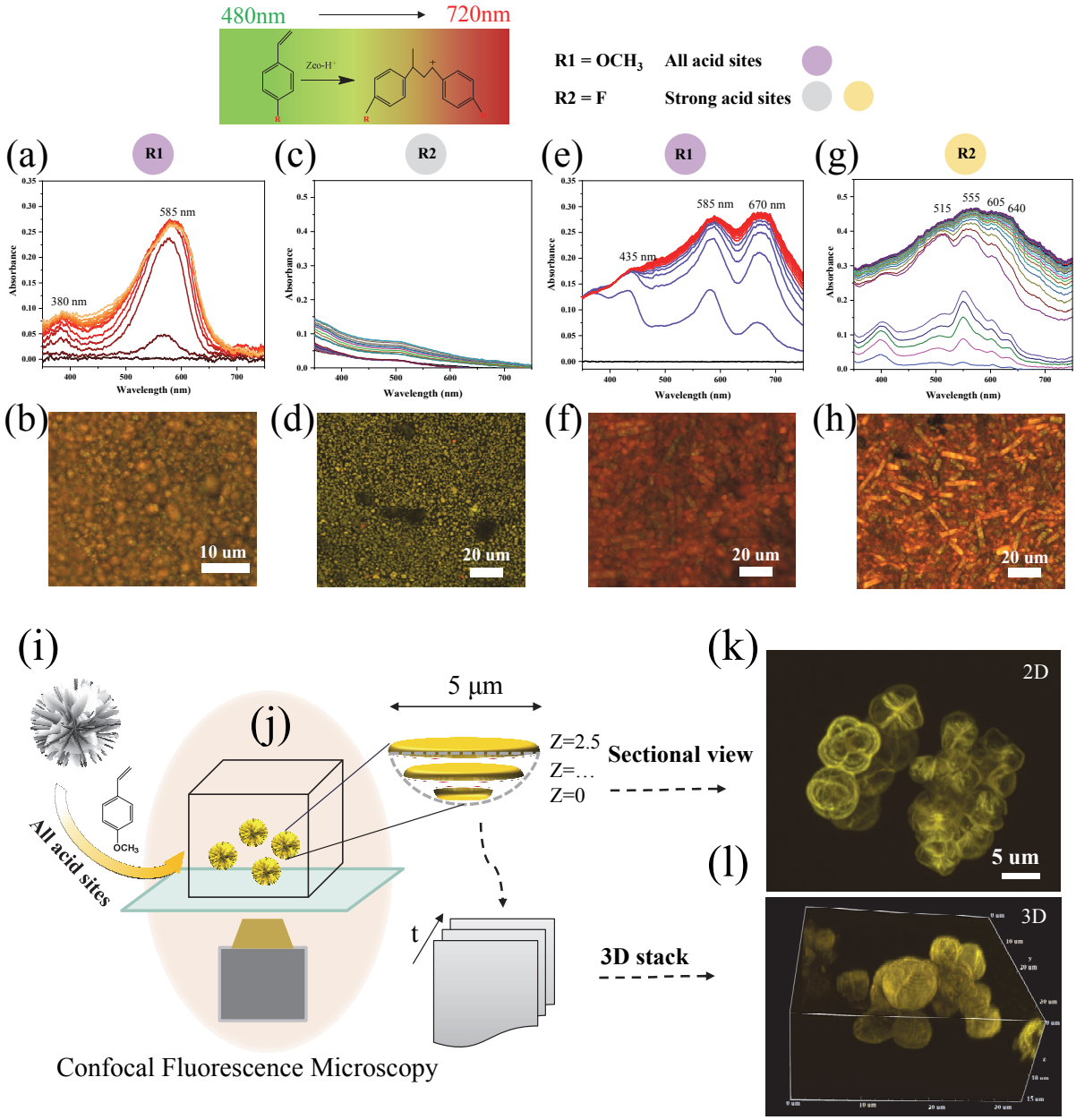

Fig. 7. *In-situ* UV-Vis time-resolved absorption spectra measured during the oligomerization of styrene derivatives over SCM-36(35) and ZSM-5 at 373 K for 3 min (a, c, e, and g). CFM images of spent SCM-36(35) and ZSM-5 zeolite after oligomerization (b, d, f, h). Where (a, b, e, f) were used 4-methoxystyrene, and (c, d, g, and h) were used 4-fluorostyrene as probe molecule. (i, j) Schematic illustration of the fluorescence microscopy selective staining approach. (k) Real cross-sectional slice CFM image of SCM-36 zeolite nanospheres. (l) CFM Image of 3D stacked cross-sectional slices of SCM-36. The probe molecules were excited at 488, 561 and 638 nm and the detection wavelength range was between 480–720 nm.

romolecular oligomerization product (Fig. 7(b)). Similarly, the appearance of absorption bands at 585 and 670 nm for ZSM-5 zeolite could be attributed to cyclic dimeric carbocations and higher oligomers (Fig. 7(e)). The crystals of ZSM-5 show a darker fluorescence distribution due to formation of multiple oligomerized products (Fig. 7(f)). However, when 4-fluorostyrene was used as the probe molecule, SCM-36 and ZSM-5 behaved completely different. The UV-Vis spectrum of SCM-36 exhibited a very faint absorption band at ~520 nm, while the CFM images of the spent catalyst showed a green fluorescence due to the unconverted small molecule and almost no red-orange fluorescence (Figs. 7(c) and (d)). The absorption bands at 515, 555, 605 and 640 nm for the highly active ZSM-5 zeolite were attributed to the presence of cyclic and liner dimeric carbocations and lager trimeric products (Fig. 7(g)). The strong orange-yellow fluorescence in the CFM images represented the presence of oligomers (Fig. 7(h)). The above results indicate that SCM-36 zeolite does not have sufficient Brönsted acid sites compared to the conventional ZSM-5 zeolite.

As fluorescent products are formed on all acid sites, their fluorescence can be used for 3D construction of zeolite SCM-36 crystal (Figs. 7(i)–(l)). Orange-yellow fluorescence spread throughout SCM-36 nanospheres after the oligomerization of 4-methoxystyrene (Figs. 7(i) and (j)). Each cross-sectional slice

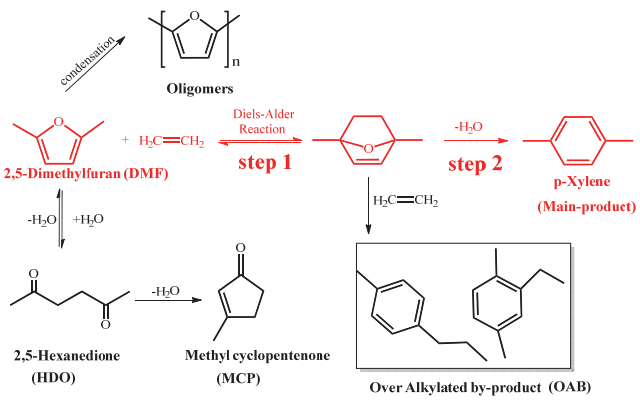

Scheme 1. Schematic illustration of the conversion of DMF to PX, including the main and side chemical reactions of the catalytic process.

of the nanosphere is clearly visible and can be seen as a dense network like a "cut orange" (Fig. 7(k)). Recording fluorescence movies (Movie S1) allow reconstructing of a high-resolution 3D image based on multiple cross-sectional slices at different time. The 3D stacked image is fully displayed by Movie S2 and is shown in Fig. 7(l). The above fluorescence microscopy measurements indicate that SCM-36 zeolite crystals are aggregates of nanoflowers with highly accessible hollow internal spatial networks. The brightly colored lines in the picture are the cross-sections of the nanosheets, and the black ones are the spaces between the nanosheets.

3.5. Catalytic performance of SCM-36 zeolite

Generally, the conversion of DMF and ethylene to produce PX takes place *via* two tandem steps: (1) the Diels-Alder cycloaddition of ethylene and DMF to form the cycloadduct intermediate, which does not depend on an active site, but is promoted primarily by confinement within zeolites [41]. (2) the subsequent dehydration of the cycloadduct to PX. The reaction pathways of this process are shown in Scheme 1. The side reactions include (a) the hydrolysis of DMF to form HDO and subsequent dehydration MCP; (b) multiple additions of ethylene feedstock resulting in formation of OAB; (c) dimerization of the aromatic products and furan feedstock to form oligomers [38,39,63].

All catalyst materials under study showed high DMF conversion after reaction for 24 h (Table 3). The proportion of weak and medium-strong acid follows the order: SCM-36 (79%) > USY (71%) > Beta (62%)> SAPO-34 (58%)> ZSM-5

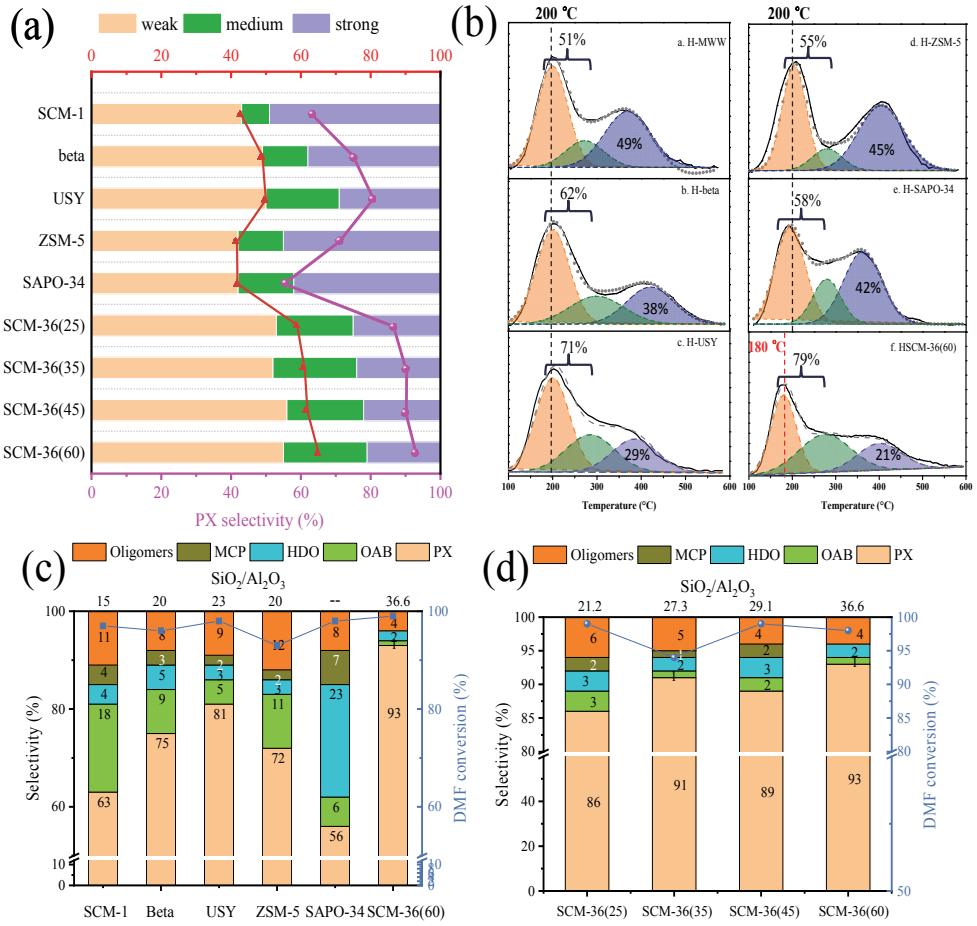

Fig. 8. (a) Acid distribution of zeolites with different structures as a function of PX selectivity. (b) Weak and strong acid ratios of different zeolite materials as demonstrated by the NH_3-TPD profile deconvolution procedure. PX selectivity (left axis) and DMF conversion (right axis) over various catalysts (c) and over SCM-36 zeolites with different bulk SiO_2/Al_2O_3 molar ratios (d). Reaction conditions: ~1.2±0.1 mol/L of DMF (1.0 g), *n*-heptane (20 ml) and zeolite (1.0 g) enclosed in the reactor and then heated to 250 °C for 24 h at 2.0 MPa with ethylene.

(55%)> MWW (51%), as shown in Figs. 8(a) and (b). Under the approximately equal conversion of DMF, the PX selectivity over different catalysts decreases in the order: SCM-36 (90%~93%) > USY (81%) > Beta (75%) > ZSM-5 (72%) > MWW (63%) > SAPO-34 (56%), which corresponds to the proportion of weak acid sites (Table 3, Figs. 8(a) and (c)). The by-products selectivity over our newly prepared SCM-36 zeolite material was lower than those over other zeolites. Alkylation and isomerization reactions that are catalyzed by strong Brönsted acid would not only reduce the para-xylene selectivity, but also cause rapid deactivation [38]. Using SCM-36 as catalyst greatly decreased the formation of OAB and oligomers, which mainly attributed to the fewer Brönsted acid sites of SCM-36 than other zeolites.

Besides, Lewis acid sites can coordinate with ethylene to promote the Diels-Alder reaction to form the cycloadduct intermediate oxanorbornene, thus accelerating the rate of step 1 [64]. Over weak and medium-strong acid sites, HDO is likely to convert into DMF (reversible reaction) and subsequently into PX. Strong acid sites turn out to be active in the condensation of HDO, resulting in the unwanted MCP condensation and carbon loss. Thus, the HDO and MCP by-products formed over SCM-36 catalysts were less than those formed over other zeolites. This is consistent with the conclusions of previous research works [31,39].

Calcined SCM-36 zeolites were used directly as catalysts in the reaction without any post-treatment procedures like acid/base treatment and noble metal ion exchange. All samples showed high selectivity to PX (Fig. 8(d)), up to 93%. Moreover, SCM-36 zeolite displayed good recyclability in the reaction. The catalytic activity of spent catalyst could be fully recovered after calcination in air (Fig. S11). The following factors may affect the performance of the catalyst in the biomass-derived DMF to PX reaction. (1) The pore structure and morphology of zeolite materials. A suitable pore system favors the production of PX while inhibiting the formation of other benzene homologues. Although the structure of SCM-36 zeolite was not solved, its channel system with pore openings concentrated at around 0.6 nm favored the production of PX. Furthermore, the two-dimensional layered structure of SCM-36 zeolite offered larger external surface and more accessible active sites than conventional zeolites with 3D structures [65,66], thus SCM-36 exhibited the most excellent performance in all herein tested zeolites. (2) The acidic properties of SCM-36 zeolite. Previous studies have indicated that to obtain catalyst with high selectivity to PX, strong acid should be avoided to reduce the formation of by-products (MCP, oligomers and so on). Besides, suitable B/L acid ratio is needed to enhance the main reaction [39]. The outstanding catalytic performance of SCM-36 could be ascribed to the above mentioned two aspects: the improved mass transfer and suitable acidic properties.

4. Conclusions

A new aluminosilicate zeolite, SCM-36, was synthesized in a composite system using TMAOH as one OSDA, together with the presence of either C_{16}PyBr or OTMAC. The obtained SCM-36 zeolite possessed a nanoflower-like morphology with a stacking manner and high surface area. This material contained a large number of weak acid sites and a small amount of strong Brönsted acid sites. The zeolite showed comparable activity and higher selectivity in the conversion of biomass-derived reactant (DMF) into PX than several other important zeolites, such as ZSM-5. The excellent catalytic performance and good recyclability of the SCM-36 zeolite would endow the new material with potential applications in a wide variety of catalytic conversion processes.

Author Contributions

All authors contributed to this work. All authors have given approval to the final version of the paper.

Declaration of Competing Interest

Graphical Abstract

Chin. J. Catal, 2023, 47: 200–213 doi: 10.1016/S1872-2067(22)64200-1

SCM-36 zeolite nanosheets applied in the production of renewable *p*-xylene from ethylene and 2,5-dimethylfuran

Duozheng Ma, Xiangcheng Li, Chuang Liu, Caroline Versluis, Yingchun Ye, Zhendong Wang *, Eelco T. C. Vogt, Bert M. Weckhuysen *, Weimin Yang *
East China University of Science and Technology, China;
Sinopec Shanghai Research Institute of Petrochemical Technology, China;
Utrecht University, the Netherlands

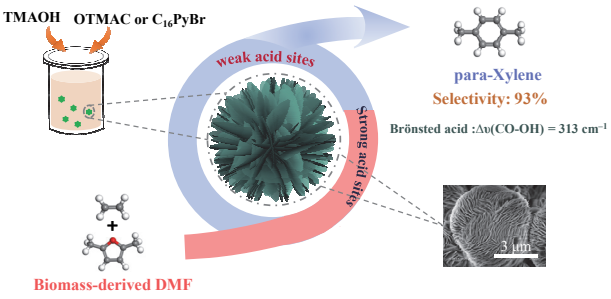

SCM-36, a new aluminosilicate zeolite with a nanosheet morphology, was synthesized with the presences of two organic structure-directing agents. It exhibited up to ~93% selectivity to para-xylene from ethylene and dimethylfuran.

The authors declare no competing financial interest.

Electronic supporting information

Supporting information is available in the online version of this article.

References

[1] A. Primo, H. Garcia, *Chem. Soc. Rev.*, **2014**, 43, 7548–7561.
[2] C. Martínez, A. Corma, *Coord. Chem. Rev.*, **2011**, 255, 1558–1580.
[3] M. E. Davis, *Nature*, **2002**, 417, 813–821.
[4] J. Li, A. Corma, J. Yu, *Chem. Soc. Rev.*, **2015**, 44, 7112–7127.
[5] http://www.iza-structure.org/databases/.
[6] B. Li, K. M. Kwok, H. C. Zeng, *ACS Appl. Mater. Interfaces*, **2021**, 13, 20524–20538.
[7] N. S. M. Rangnekar, K. V. Agrawal, B. Topuz, P. Kumar, Q. Guo, I. Ismail, A. Alyoubi, S. Basahel, K. Narasimharao, C. W. Macosko, K. A. Mkhoyan, S. Al-Thabaiti, B. Stottrup, M. Tsapatsis, *Angew. Chem. Int. Ed.*, **2015**, 54, 6571–6575.
[8] L. Xu, J. Sun, *Adv. Energy Mater.*, **2016**, 6, 1600441.
[9] M. Choi, K. Na, J. Kim, Y. Sakamoto, O. Terasaki, R. Ryoo, *Nature*, **2009**, 461, 246–249.
[10] Y. Ma, X. Tang, J. Hu, Y. Ma, W. Chen, Z. Liu, S. Han, C. Xu, Q. Wu, A. Zheng, L. Zhu, X. Meng, F. S. Xiao, *J. Am. Chem. Soc.*, **2022**, 144, 6270–6277.
[11] R. M. Barrer, *J. Chem. Soc.*, **1948**, 127–132.
[12] R. F. Lobo, S. I. Zones, M. E. Davis, *J. Inclusion Phenom. Mol. Recognit. Chem.*, **1995**, 21, 47–78.
[13] D. Ma, W. Fu, C. Liu, J. Liang, Z. Yuan, W. Tao, Z. Wang, W. Yang, *ACS Omega*, **2021**, 6, 23598–23606.
[14] G. J. Lewis, D. Y. Jan, B. J. Mezza, J. G. Moscoso, M. A. Miller, B. A. Wilson, S. T. Wilson, *Stud. Surf. Sci. Catal.*, **2004**, 154, 118–125.
[15] W. Fu, Z. Yuan, S. Jin, W. Liu, Z. Wang, C. Wang, Y. Wang, W. Yang, M.-Y. He, *Chin. J. Catal.*, **2019**, 40, 856–866.
[16] D. Y. Jan, G. J. Lewis, T. M. Mezza, J. G. Moscoso, R. L Patton,.; M. P. Koljack, P. V. Tota, *Stud. Surf. Sci. Catal.*, **2004**, 154, 1332–1340.
[17] N. Nakazawa, T. Ikeda, N. Hiyoshi, Y. Yoshida, Q. Han, S. Inagaki, Y. Kubota, *J. Am. Chem. Soc.*, **2017**, 139, 7989–7997.
[18] D. Ma, X. Li, J. Liang, Z. Wang, W. Yang, *Microporous Mesoporous Mater.*, **2022**, 339, 112029.
[19] Y. Ji, Y. Wang, B. Xie, F.-S. Xiao, *Comments Inorg. Chem.*, **2016**, 36, 1–16.
[20] K. Suzuki, T.Hayakawa, *Microporous Mesoporous Mater.*, **2005**, 77, 131–137.
[21] E. Bello-Jurado, D. Schwalbe-Koda, M. Nero, C. Paris, T. Uusimaki, Y. Roman-Leshkov, A. Corma, T. Willhammar, R. Gomez-Bombarelli, M. Moliner, *Angew. Chem. Int. Ed.*, **2022**, 61, e202201837.
[22] V. J. Margarit, M. E. Martinez-Armero, M. T. Navarro, C. Martinez, A. Corma, *Angew. Chem. Int. Ed.*, **2015**, 54, 13724–13728.
[23] R. García, L. Gómez-Hortigüela, J. Pérez-Pariente, *Catal. Today*, **2012**, 179, 16–26.
[24] R. K. S. Almeida, L. Gómez-Hortigüela, A. B. Pinar, J. Peréz-Pariente, *Microporous Mesoporous Mater.*, **2016**, 232, 218–226.
[25] A. B. Pinar, L. Gómez-Hortigüela, L. B. McCusker, J. Pérez-Pariente, *Chem. Mater.*, **2013**, 25, 3654–3661.
[26] H. Xu, J. Zhu, L. Zhu, E. Zhou, C. Shen, *Molecules*, **2020**, 25, 3722.
[27] A. B. Pinar, L. Gomez-Hortiguela, J. Perez-Pariente, *Chem. Mater.*, **2007**, 19, 5617–5626.
[28] R. Martínez-Franco, M. Moliner, J. R. Thogersen, A. Corma, *ChemCatChem*, **2013**, 5, 3316–3323.
[29] D. Rima, D. Djamal, D. Fatiha, *Mater. Res. Express*, **2019**, 6, 035017.
[30] C. T. Nimlos, A. J. Hoffman, Y. G. Hur, B. J. Lee, J. R. Di Iorio, D. D. Hibbitts, R. Gounder, *Chem. Mater.*, **2020**, 32, 9277–9298.
[31] C.-C. Chang, S. K. Green, C. L. Williams, P. J. Dauenhauer, W. Fan, *Green Chem.*, **2014**, 16, 585–588.
[32] C.-C. Chang, H. Je Cho, J. Yu, R. J. Gorte, J. Gulbinski, P. Dauenhauer, W. Fan, *Green Chem.*, **2016**, 18, 1368–1376.
[33] T. Dai, C. Li, L. Li, Z. K. Zhao, B. Zhang, Y. Cong, A. Wang, *Angew. Chem. Int. Ed.*, **2018**, 57, 1808–1812.
[34] T. W. Lyons, D. Guironnet, M. Findlater, M. Brookhart, *J. Am. Chem. Soc.*, **2012**, 134, 15708–15711.
[35] Y. Xiao, Q. Meng, X. Pan, C. Zhang, Z. Fu, C. Li, *Green Chem.*, **2020**, 22, 4341–4349.
[36] Y.-T. Cheng, J. Jae, J. Shi, W. Fan, G. W. Huber, *Angew. Chem. Int. Ed.*, **2012**, 51, 1387–1390.
[37] P. T. Do, J. R. McAtee, D. A. Watson, R. F. Lobo, *ACS Catal.*, **2013**, 3, 41–46.
[38] H. J. Cho, L. Ren, V. Vattipalli, Y.-H. Yeh, N. Gould, B. Xu, R. J. Gorte, R. Lobo, P. J. Dauenhauer, M. Tsapatsis, W. Fan, *ChemCatChem*, **2017**, 9, 398–402.
[39] X. Feng, Z. Cui, Y. Bao, H. Chu, X. Wu, C. Shen, T. Tan, *J. Catal.*, **2021**, 401, 214–223.
[40] J.-C. Kim, T.-W. Kim, Y. Kim, R. Ryoo, S.-Y. Jeong, C.-U. Kim, *Appl. Catal. B*, **2017**, 206, 490–500.
[41] C. L. Williams, C.-C. Chang, P. Do, N. Nikbin, S. Caratzoulas, D. G. Vlachos, R. F. Lobo, W. Fan, P. J. Dauenhauer, *ACS Catal.*, **2012**, 2, 935–939.
[42] Z. Wang, M. O. Cichocka, Y. Luo, B. Zhang, H. Sun, Y. Tang, W. Yang, *Chin. J. Catal.*, **2020**, 41, 1062–1066.
[43] C. A. Emeis, *J. Catal.*, **1993**, 141, 347–354.
[44] M. Peng, Z.-Q. Wang, J. Huang, M. Shen, J. Jiang, H. Xu, Y. Ma, B. Hu, X.-Q. Gong, H.-H. Wu, P. Wu, *Chem. Mater.*, **2021**, 33, 6934–6941.
[45] Q.-F. Lin, Z. R. Gao, C. Lin, S. Zhang, J. Chen, Z. Li, X. Liu, W. Fan, J. Li, X. J. S. Chen, *Science*, **2021**, 374, 1605–1608.
[46] A. T. Bell, *Colloids Surf. A*, **1999**, 158, 221–234.
[47] H. Gies, U. Müller, B. Yilmaz, T. Tatsumi, B. Xie, F.-S. Xiao, X. Bao, W. Zhang, D. D. Vos, *Chem. Mater.*, **2011**, 23, 2545–2554.
[48] A. G. Stepanov, *Zeolites Zeolite-Like Mater.*, **2017**, 137–188.
[49] J. Liang, Y. Wang, X. Li, M. Xu, S. Shen, C. Liu, W. Fu, W. Tao, Z. Yuan, Z. Wang, W. Yang, *Microporous Mesoporous Mater.*, **2021**, 328, 111448.
[50] O. Kresnawahjuesa, D. H. Olson, R. J. Gorte, G. H. Kühl, *Microporous Mesoporous Mater.*, **2002**, 51, 175–188.
[51] I. L. C. Buurmans, J. Ruiz-Martinez, S. L. van Leeuwen, D. van der Beek, J. A. Bergwerff, W. V. Knowles, E. T. C. Vogt, B. M. Weckhuysen, *Chem. Eur. J.*, **2012**, 18, 1094–1011.
[52] E. Soghrati, T. K. C. Ong, C. K. Poh, S. Kawi, A. Borgna, *Appl. Catal. B*, **2018**, 235, 130–142.
[53] B. O. Bonelli, J. D. Chen, A. Galarneau, F. Di Renzo, F. Fajula, E. Garrone, *Microporous Mesoporous Mater.*, **2004**, *67*, 95–106.
[54] H. Knözinger, S. Huber, *J. Chem. Soc., Faraday Trans.*, **1998**, 94, 2047–2059.
[55] A. Zecchina, S. Bordiga, G. Spoto, D. Scarano, G. Petrini, G. Leofanti, M. Padovan, C. O. Areàn, *J. Chem. Soc., Faraday Trans.*, **1992**, 88, 2959–2969.
[56] J. Goetze, B. M. Weckhuysen, *Catal. Sci. Technol.*, **2018**, 8, 1632–1644.
[57] A. Zecchina, C. O. Areán, *Chem. Soc. Rev.*, **1996**, 25, 187–197.
[58] S. Valencia, *Molecules*, **2021**, 26, 730.
[59] L. Kubelková, S. Beran, J. A. Lercher, *Zeolites*, **1989**, 9, 539–543.
[60] I. L. C. Buurmans, E. A. Pidko, J. M. de Groot, E. Stavitski, R. A. van

Santen, B. M. Weckhuysen, *Phys. Chem. Chem. Phys.*, **2010**, 12, 7032–7040.
[61] A.-E. Nieuwelink, J. C. Vollenbroek, R. M. Tiggelaar, J. G. Bomer, A. van den Berg, M. Odijk, B. M. Weckhuysen, *Nat. Catal.*, **2021**, 4, 1070–1079.
[62] M. H. Kox, E. Stavitski, B. M. Weckhuysen, *Angew. Chem. Int. Ed.*, **2007**, 46, 3652–3655.
[63] R. E. Patet, N. Nikbin, C. L. Williams, S. K. Green, C.-C. Chang, W. Fan, S. Caratzoulas, P. J. Dauenhauer, D. G. Vlachos, *ACS Catal.*, **2015**, 5, 2367–2375.
[64] N. Nikbin, P. T. Do, S. Caratzoulas, R. F. Lobo, P. J. Dauenhauer, D. G. Vlachos, *J. Catal.*, **2013**, 297, 35–43.
[65] K. S. Arias, M. J. Climent, A. Corma, S. Iborra, *ACS Sustainable Chem. Eng.*, **2016**, 4, 6152–6159.
[66] M. V. Opanasenko, W. J. Roth, J. Čejka, *Catal. Sci. Technol.*, **2016**, 6, 2467–2484.

SCM-36分子筛纳米片用于乙烯和2,5-二甲基呋喃转化制可再生对二甲苯

马多征[a,b,c], 李相呈[b], 刘 闯[b], Caroline Versluis [c], 叶迎春[b], 王振东[b,c,*], Eelco T. C. Vogt [c], Bert M. Weckhuysen [c,*], 杨为民[a,b,*]

[a]华东理工大学化工学院, 上海200237, 中国
[b]中国石化上海石油化工研究院, 绿色化工与工业催化国家重点实验室, 上海201208, 中国
[c]乌得勒支大学德拜纳米材料科学研究所, 可持续与循环化学研究所, 无机化学与催化组, 乌得勒支, 荷兰

摘要: 分子筛是一类重要的结晶多孔材料, 广泛应用于化学工业. 开发新型分子筛特别是硅铝酸盐分子筛, 一直是该领域的研究热点. 分子筛的晶化过程一般需要结构导向剂的参与, 包括碱(土)金属离子为代表的无机阳离子, 有机胺或季铵盐为代表的有机物以及分子筛晶种. 采用两种及以上结构导向剂的分子筛合成策略, 具有调节分子筛骨架原子、晶体形貌和化学组成的作用, 是开发新分子筛的有效手段. 对二甲苯(PX)是合成对苯二甲酸乙二醇酯(PET)的重要原料. PX 主要来源于石油资源, 开发基于生物质原料生产 PX 的技术有利于缓解日益严峻的环境和能源危机.

本文采用两种有机结构导向剂, 以四甲基氢氧化铵(TMAOH)为有机结构导向剂, 同时向体系中加入十六烷基溴化吡啶(C_{16}PyBr)或正辛基三甲基氯化铵(OTMAC), 合成了一种新型铝硅酸盐分子筛, 命名为 SCM-36(Sinopec Composite Material No.36). SCM-36 分子筛具有独特的 X 射线粉末衍射谱图(XRD)和纳米片状形貌. 原位 XRD 结果表明, SCM-36 分子筛在焙烧过程中由于晶胞收缩而导致衍射峰的偏移. 扫描电子显微镜(SEM)、原子力显微镜以及共聚焦荧光成像显微镜表征结果表明, 分子筛为纳米片形貌, 厚度为 6.9–14.9 nm. N_2 和 Ar 物理吸附-脱附结果表明, SCM-36 分子筛的 BET 表面积为 355 m^2/g, 其具有 0.59 nm 和 0.67 nm 左右孔尺寸的微孔孔道. 两种有机结构导向剂都进入了分子筛孔道, 在焙烧时于不同的温度区间发生分解. 原位 CO 傅里叶变换红外光谱结果表明, SCM-36 的 Brönsted 酸强度($\Delta\upsilon$(CO···OH) = 313 cm^{-1})与 ZSM-5 相当. 采用原位紫外可见光吸收光谱监测 4-甲氧基苯乙烯和 4-氟苯乙烯的低聚探针反应过程, 证实了 SCM-36 分子筛同时具有强酸和弱酸, 且以弱酸为主的酸性质.

在催化 DMF 和乙烯制备 PX 的反应中, SCM-36 分子筛不仅表现出与传统分子筛(ZSM-5, Beta)相当的高转化率, 而且表现出更高的 PX 选择性(93%). 其较好的催化性能归因于该分子筛良好的扩散性能和适宜的酸性质. 且 SCM-36 分子筛的稳定性较好, 可重复使用. 综上, 利用双有机结构导向剂合成分子筛是开发新分子筛的有效策略, 采用该策略合成的 SCM-36 纳米片分子筛具有潜在的应用价值.

关键词: 分子筛; 硅铝酸盐; SCM-36; 原位光谱; 对二甲苯; 生物质

收稿日期: 2022-10-24. 接受日期: 2022-11-25. 上网时间: 2023-03-20.
* 通讯联系人. 电子信箱: wangzd.sshy@sinopec.com (王振东), B.M.Weckhuysen@uu.nl (B. Weckhuysen), yangwm.sshy@sinopec.com (杨为民).
基金来源: 国家自然科学基金(21972168, 21802168); 国家留学基金委(CSC); 中国石油化工股份有限公司.